

Combined model for the H-mode pedestal and ELMs

A Y Pankin¹, I Voitsekhovitch², G Bateman³, A Dnestrovski⁴,
G Janeschitz⁵, M Murakami⁶, T Osborne⁷, A H Kritiz³, T Onjun³,
G W Pacher⁸ and H D Pacher⁹

¹ SAIC, 10260 Campus Point Dr., San Diego, CA 92069, USA

² JET-UKAEA, Culham Science Centre, UK

³ Lehigh University, Bethlehem, PA 18015, USA

⁴ Kurchatov Institute, Russian Federation

⁵ FZK-PL-Fusion, Karlsruhe, Germany

⁶ Oak Ridge National Laboratory, Oak Ridge, TN 37831, USA

⁷ General Atomics, San Diego, CA 92186, USA

⁸ Hydro-Québec, Varennes, Québec, Canada

⁹ INRS, Québec, Canada

AQ1

E-mail: pankin@haven.adnc.net

Received 16 June 2004, in final form 21 October 2004

Published

Online at stacks.iop.org/PPCF/46

doi:10.1088/0741-3335/46/1/...

Abstract

A model is developed for use in integrated modelling codes to predict the height, width and shape of the H-mode pedestal as well as the frequency and width of edge localized modes (ELMs). The model for the H-mode pedestal in tokamak plasmas is based on flow shear reduction of anomalous transport, while the periodic ELM crashes are triggered by MHD instabilities. The formation of the pedestal and the L–H transition in this model are the direct result of $\vec{E}_r \times \vec{B}$ flow shear suppression of transport. Suppression of the anomalous transport enhances the role of neoclassical transport in the pedestal region. The ratio of suppression of anomalous thermal transport in electron and ion channels controls the ratio of electron to ion temperature at the top of the pedestal. Two mechanisms for triggering ELMs are considered. ELMs are triggered by ballooning modes if the pressure gradient exceeds the ballooning limit or by peeling modes if the edge current density exceeds the peeling mode criterion. The models for the pedestal and ELMs are used in a predictive integrated modelling code to follow the time evolution of tokamak discharges from L-mode through the transition from L-mode to H-mode, with the formation of the H-mode pedestal, and, subsequently, the triggering of ELMs. The objective is to produce self-consistent predictions of the width, height and shape of the H-mode pedestal and the frequency of ELMs. The dependencies of pedestal temperature, pedestal width and ELM frequency as a function of plasma heating power, magnetic field and density are discussed.

1. Introduction

An objective of integrated modelling of tokamak plasmas is to predict plasma profiles and discharge performance within a code that self-consistently computes sources and sinks, large-scale instabilities, as well as neoclassical and anomalous transport coefficients in the plasma core and at the plasma edge. The formation of the high confinement mode (H-mode) pedestal has a significant effect on the entire plasma profile.

There are a number of instabilities that are believed to be responsible for anomalous thermal transport [1], such as the ion and electron temperature gradient (ITG and ETG) modes, trapped electron modes (TEMs) and resistive ballooning modes. These modes provide contributions to transport that are different in the plasma core and at the plasma edge. For example, ITG and TEM modes are major contributors to transport in the plasma core, while the resistive ballooning modes contribute at the plasma edge. The different instabilities are suppressed by the flow shear at different rates. In the pedestal, anomalous transport is strongly suppressed and the role of neoclassical transport becomes important [2, 3].

The stabilizing effect of the $\vec{E}_r \times \vec{B}$ shear on the drift turbulence is well recognized and established [4–8]. There are two widely accepted models for the suppression of drift turbulence in the plasma core, the Hahn–Burrell model and the Hamaguchi–Horton model. These models have been used to predict the formation of internal transport barriers (ITBs) [9]. The Hahn–Burrell model states that the drift turbulence is completely suppressed if the Hahn–Burrell shearing rate $\omega_{E \times B}$,

$$\omega_{E \times B} \equiv \left| \frac{RB_\theta}{B_\phi} \frac{\partial}{\partial r} \left(\frac{E_r}{RB_\theta} \right) \right| \quad (1)$$

is greater than the maximum growth rate of the drift modes [6]. In equation (1), B_θ and B_ϕ are poloidal and toroidal components of the magnetic field, R is the major radius and E_r is the radial component of electric field. The Hamaguchi–Horton model states that the drift mode transport coefficients are reduced by the factor

$$\mathcal{F}_s = \frac{1}{1 + (\mathcal{W}/\mathcal{W}_{\text{crit}})^2}, \quad (2)$$

where $\mathcal{W}_{\text{crit}}$ is the critical value that is close to unity and \mathcal{W} is the Hamaguchi–Horton shear parameter [5]. The Hamaguchi–Horton shear parameter takes into account the effect of magnetic shear in addition to the $\vec{E}_r \times \vec{B}$ flow shear,

$$\mathcal{W} \approx R \sqrt{\frac{m_i}{T_e}} \left| \frac{\partial}{\partial \psi} \left(\frac{E_r}{RB_\theta} \right) \left(\frac{\partial \ln q}{\partial \psi} \right)^{-1} \right|, \quad (3)$$

where m_i is the ion mass, T_e is the electron temperature, q is the local safety factor and ψ is the magnetic stream function.

The effect of $\vec{E}_r \times \vec{B}$ flow shear on the edge turbulence has been studied by Shaing *et al* [10] and Zhang and Mahajan [11]. They found that the flow shear reduces the fluctuation level by a term proportional to $|dv_\theta/dr|^2$ (where v_θ is the $\vec{E}_r \times \vec{B}$ poloidal velocity) in the small flow shear regime. In a more general treatment of weak turbulence theory, the turbulence level is reduced by the factor $1 + 2\alpha^{-2}(|dv_\theta/dr|\tau_c)^2$. Here τ_c is the decorrelation time without flow shear and α is a measure of anisotropy of the k spectrum. Recent studies by Figarella *et al* [12] have shown that the anomalous transport caused by the resistive pressure-gradient driven turbulence is suppressed by rotation shear by the following rate:

$$F_s = \frac{1}{1 + (\tau_c \hat{\omega}_{E \times B})^\gamma}, \quad (4)$$

where τ_c is the correlation time of fluctuations for the case without flow, $\hat{\omega}_{E \times B}$ is the normalized $\vec{E}_r \times \vec{B}$ flow shear rate and γ is a constant, which is close to 2. A similar model for the ITG turbulence suppression has been developed by Zolotukhin *et al* [13], Janeschitz *et al* [14] and Pacher *et al* [15]. In the latter studies [14, 15], a magnetic shear dependence was introduced into the flow shear suppression function based on experimental observations of pedestal characteristics in several tokamaks and which included a dependence on triangularity [16]. This shear suppression function has the form

$$F_s = \frac{\mathcal{G}(s)}{1 + (\omega_{E \times B} / \hat{\gamma}_{\text{ITG}})^2}, \quad (5)$$

where $\mathcal{G}(s)$ is the magnetic shear stabilization function, $\hat{\gamma}_{\text{ITG}}$ is the volume average of ITG growth rate, without stabilization, inside 0.9 of the minor radius. The stabilizing magnetic field shear effect is related to the dependence of the ITG thermal diffusivity on the magnetic field [16]. Some analytical derivations also suggest that, for high radial ITG mode numbers, the thermal diffusivity is reduced with increasing magnetic shear [17]. The magnetic shear stabilization function used by Zolotukhin *et al* [13] has the form $\mathcal{G}(s) = s^{-1.8}$. An additional threshold dependence has been introduced by Pacher *et al* [15] into the magnetic shear stabilization function $\mathcal{G}(s) = \min(1, (s - s_{\text{th}}))^{-2}$. The threshold value s_{th} is determined by calibration with experimental data. The magnetic shear factor $\mathcal{G}(s)$ is not needed if the magnetic shear stabilization effect is already included in the transport model, as it is in the Weiland model used in this paper [18].

The combined magnetic and $\vec{E}_r \times \vec{B}$ flow shear effect on the ion thermal transport has been studied by Voitsekhovitch *et al* [19]. The proposed exponential shear functions have been successfully used for the predictive analysis of some advanced tokamak scenarios with ITBs on TFTR, DIII-D and JET tokamak devices. Both anomalous and neoclassical ion thermal transport have been suppressed (in some cases to levels below the conventional neoclassical level) in order to adequately reproduce the core evolution of the temperature.

A model for edge localized modes (ELMs) has been implemented recently in the JETTO transport code. This work is described in a series of recent publications by Lönnroth *et al* [20–22] as well as Onjun *et al* [23, 24]. In the model in which ELMs are triggered by ballooning or peeling modes, transport is computed using the JET transport (mixed Bohm/gyro-Bohm) model. In contrast to the approach taken in this paper, the pedestal width is prescribed and the ion thermal neoclassical transport at the top of the pedestal is used for all of the channels of transport (even electron thermal transport) throughout the pedestal. The changes in the plasma profiles during each ELM crash are produced by transiently increasing the transport in the pedestal in that model.

Integrated modelling studies that self-consistently take into account the effects of the plasma edge have been developing during the last decade [13–15, 20–28]. Some of these simulations are rather comprehensive and take into account MHD equilibrium, turbulent anomalous radial transport, neutral gas transport, atomic and molecular physics and plasma–wall interactions. At the same time, many open questions remain. Examples of such questions are: How are the different short and long wavelength modes suppressed by the $\vec{E}_r \times \vec{B}$ flow shear? Is there a single model for flow shear suppression of transport in the plasma core and at the plasma edge? How does the H-mode pedestal recover after an ELM crash? What is the effect of ELMs on the pedestal characteristics? With the issue of particle transport left aside for future work, this paper will address some of these questions, namely the issue of anomalous thermal transport suppression, formation of the pedestal, L–H transition, triggering of ELMs and the effect of ELMs on the pedestal characteristics.

This paper is organized in the following manner. In section 2.1, a model for the H-mode pedestal is introduced. The model is based on the $\vec{E}_r \times \vec{B}$ flow shear suppression of anomalous thermal transport. A description of the ELM triggering criteria is given in section 2.2. Two triggering mechanisms are considered: ELM crashes are caused either by ballooning mode instabilities or by peeling mode instabilities. The combined model for the H-mode pedestal and the ELMs has been implemented in the ASTRA transport code [29] and is used in this paper to predict the L–H transition, the height, width and shape of the H-mode pedestal, as well as the frequency of ELMs. Section 3 contains a description of the implementation and includes results of simulations of a reference case. The reference case has plasma parameters and geometry appropriate for a DIII-D discharge [30]. Results of simulations, in which the plasma density, magnetic field and heating power are varied, are presented in section 4, and the derived scalings are compared with experimental observations. Discussion of the results and conclusions are presented in section 5.

2. Combined model for H-mode pedestal and ELM crashes

2.1. Suppression of anomalous thermal transport due to the $\vec{E}_r \times \vec{B}$ flow shear

A model is described in this section for the suppression of anomalous transport by the $\vec{E}_r \times \vec{B}$ flow shear. The objective is to develop a model for the flow shear suppression of anomalous transport at the plasma edge and for triggering ELM crashes. When the models for the anomalous transport suppression, which are described in the introduction of this paper, are compared, it can be seen that suppression rates in equations (4) and (5) resemble the Hamaguchi–Horton suppression rate in equation (2). The flow shear suppression function in the form given by equation (5) was used to model the formation of edge transport barriers (ETBs) by Zolotukhin *et al* [13] and Janeschitz *et al* [14]; whereas, the suppression rate in equation (2) was used to predict the formation of ITB [9]. However, the shear suppression model used to describe the formation of edge barriers was not extended and applied to the core and, similarly, the model used to describe the formation of ITBs was not extended and applied at the plasma edge. As noted above, the intent of this study is to derive a shear suppression function suitable for the entire plasma profile in order to use the derived shear suppression function in a predictive integrated modelling code. While it is desirable to have a single suppression function that allows the description of internal and external transport barriers, note that the core and edge turbulence may be in different regimes (quasi-linear versus strongly non-linear), and it may be necessary to use different shear functions for stabilizing different modes.

Different drift instabilities are suppressed by the $\vec{E}_r \times \vec{B}$ flow shear at different rates. For example, short wavelength ETG modes are almost unaffected by the flow shear, while longer wavelength ITG and TEM modes are strongly suppressed by sufficiently high levels of flow shear [3]. Consequently, it is important to separate the contributions of the different instabilities that drive anomalous transport. In the Multi-Mode transport model [18], the contributions to transport resulting from the ITG and TEM modes, kinetic ballooning and resistive ballooning modes are all computed separately. The ITG and TEM thermal diffusivities, $\chi_{\text{TGM}}^{(j)}$, which are referred to as drift temperature gradient driven modes (TGM) later in this paper, are computed with the Weiland model [18, 31, 32]. The Weiland model uses the quasilinear fluid equations with magnetic drifts for each plasma species and takes into account finite Larmor radii, collisions, finite β , electromagnetic effects, impurities and fast ions. The Guzdar–Drake model [33] is used for the computation of resistive ballooning diffusivities, $\chi_{\text{RB}}^{(j)}$. The Multi-Mode model also uses a simple analytical expression for computation of the kinetic ballooning

instabilities, $\chi_{\text{KB}}^{(j)}$. The contribution from the ETG mode is not part of the original Multi-Mode model, but these modes can be important because there is minimal suppression of the modes by the $\vec{E}_r \times \vec{B}$ flow shear. The Horton model [34], which is based on a hydrodynamic theory of short wavelength drift turbulence with electromagnetic effects, can be used for the computation of the ETG thermal diffusivities, $\chi_{\text{ETG}}^{(j)}$. Both the Multi-Mode transport model and the Horton model are calibrated against experimental data and each model has its own calibration constant. Neoclassical thermal contributions, χ_{neo} , are computed using the NCLASS module [35]. It should be noted that in the pedestal region, where the plasma gradients are very steep, the characteristic scale lengths of the temperatures and densities are of the order of the ion banana width and conventional neoclassical theory is close to the limits of its applicability. While it might be important for future integrated predictive transport modelling to enhance the neoclassical theory by inclusion of various effects intrinsic to the pedestal physics, such as the effects of the short gradient scale lengths and more frequent collisions with neutrals from the first wall, recent comparisons between theoretical predications and the observed transport in the H-mode pedestal in the DIII-D tokamak have shown that the conventional neoclassical theory is in reasonable agreement with the experimental data [3].

In order to take into account that different instabilities are suppressed by the $\vec{E}_r \times \vec{B}$ flow shear at different rates, separate shear suppression functions $F_l^{(j)}$ are used. The contributions from the different instabilities together with the neoclassical thermal diffusivity, χ_{neo} , constitute the total ion and electron thermal diffusivity:

$$\chi_i = F_{\text{TGM}}^{(i)} \chi_{\text{TGM}}^{(i)} + F_{\text{RB}}^{(i)} \chi_{\text{RB}}^{(i)} + \chi_{\text{KB}}^{(i)} + \chi_{\text{neo}}^{(i)}, \quad (6)$$

$$\chi_e = F_{\text{TGM}}^{(e)} \chi_{\text{TGM}}^{(e)} + F_{\text{RB}}^{(e)} \chi_{\text{RB}}^{(e)} + \chi_{\text{KB}}^{(e)} + \chi_{\text{ETG}}^{(e)} + \chi_{\text{neo}}^{(e)}, \quad (7)$$

where

$$F_l^{(j)} = \frac{1}{1 + \alpha_l^{(j)} (\omega_{E \times B} \tau_{lj})^2}, \quad l = (\text{TGM}, \text{RB}), \quad j = (\text{ions}, \text{electrons}) \quad (8)$$

and where $\chi_l^{(j)}$ is the anomalous thermal diffusivity; τ_{lj} is the turbulence correlation time, which is estimated as $\tau_{lj} = L_l^2 / \chi_l^{(j)}$. The coefficients $\alpha_l^{(j)}$ are calibrated in section 3. L_l is the turbulence characteristic scale length. For the TGM modes, L_{TGM} is set equal to the gyro-radius ρ_s , and for the resistive ballooning modes, L_{RB} is defined as [36]

$$L_{\text{RB}} = 2\pi q(a) R \left(\frac{2ne^2 \eta_{\parallel} \rho_s}{m_e \Omega_e \sqrt{2R} L_n} \right)^{1/2}, \quad (9)$$

where $q(a)$ is the safety factor at the plasma edge, η_{\parallel} is the classical resistivity, Ω_e is the electron gyro-frequency and $L_n = -dr/d \ln n$ is the scale length of the density gradient. Note that the shear suppression function given by equation (8) does not include the magnetic shear stabilization term included in equation (5). The Weiland model for the TGM modes already includes the effect of magnetic shear. Furthermore, Figarella *et al* [12] showed that the formation of the H-mode pedestal, for the case of resistive ballooning turbulence and varying biasing field, can be explained exclusively by the $\vec{E}_r \times \vec{B}$ flow shear suppression. It should be noted, however, that the magnetic shear profile was not changed in that study in order to demonstrate that magnetic shear does not play a significant role in the formation of the pedestal. Finally, as noted in the Introduction, a separate magnetic shear stabilization factor is not needed, since magnetic shear stabilization is already part of the Weiland model used in this paper [18]. In this study, the formation of an ETB, employing only suppression resulting from the $\vec{E}_r \times \vec{B}$ flow shear, is tested for one magnetic geometry.

The radial electric field, E_r , which determines the $\vec{E}_r \times \vec{B}$ shear rate given by equation (1), is computed from the first order radial force balance equation:

$$E_r = \frac{1}{Z_i e n_i} \frac{\partial p_i}{\partial r} - v_\theta B_\phi + v_\phi B_\theta, \quad (10)$$

where v_θ and v_ϕ are the poloidal and toroidal velocities, respectively. The neoclassical expression for the poloidal rotation velocity in collisionless regime is used [37]:

$$v_\theta = \frac{0.8839 f_c}{e Z_i (0.3477 + 0.4058 f_c)} \frac{B_\phi}{B^2} \frac{\partial T_i}{\partial r}, \quad (11)$$

where $f_c = 1 - 1.46\epsilon^{1/2} + 0.46\epsilon^{3/2}$ is the average fraction of circulating particles and $\epsilon = r/R$ is the aspect ratio. The toroidal rotation velocity is taken from experimental data in the studies described in sections 3 and 4.

2.2. Model for ELMs

ELMs are among the determinant factors at the plasma edge that affect the whole plasma profile, since up to 10% of the plasma energy can be removed by a single ELM crash. An ELM crash can be initiated either by a pressure driven ballooning instability or by a current driven peeling instability [38–40]. A ballooning instability causes an ELM crash if the normalized pressure gradient, α , exceeds a critical value, α_{cr} , at any location within the pedestal region. The normalized pressure gradient in an arbitrary geometry can be defined as

$$\alpha = \frac{\mu_0}{2\pi^2} \frac{\partial p}{\partial \psi} \frac{\partial V}{\partial \psi} \left(\frac{V}{2\pi^2 R} \right)^{1/2}, \quad (12)$$

where V is the plasma volume and ψ is the poloidal flux. This expression reduces to the conventional definition in the cylindrical geometry

$$\alpha = -2\mu_0 R \left(\frac{q}{B} \right)^2 \left(\frac{dp}{dr} \right). \quad (13)$$

Parametrized dependencies for the stability threshold are generally used in transport codes, rather than determining the critical value by using a comprehensive MHD stability analysis code. In this study, it is assumed that the plasma is in the first ballooning stability region. An ELM crash occurs when α exceeds α_{cr} , where the value of α_{cr} is computed using the analytic expression [25]

$$\alpha_{cr} = 0.4s \left(1 + \kappa_{95}^2 (1 + 5\delta_{95}^2) \right), \quad (14)$$

where s is the magnetic shear, κ_{95} and δ_{95} are the elongation and triangularity at the 95% flux surface. A different expression for α_{cr} would be appropriate if the more general expression for α given by equation (12) were used. This value for α_{cr} is likely to be somewhat lower.

A peeling instability causes an ELM crash if the following condition is satisfied [41]:

$$\sqrt{1 - 4D_M} < C_\kappa \left[1 + \frac{1}{\pi q'} \oint \frac{\mu_0 J_\parallel B}{R^2 B_p^3} dl \right], \quad (15)$$

where D_M is the Mercier coefficient proportional to the pressure gradient, B_p is the poloidal component of the magnetic field, q' is the derivative of the safety factor with respect to the poloidal flux and C_κ is the coefficient that is introduced in order to reproduce the stabilizing effects of the vacuum region and plasma shaping. The combined effects of ballooning and peeling criteria are shown as a schematic diagram in figure 1. The part of the curve to the left of point A in figure 1 represents the peeling mode stability criterion given by equation (15); the part of the curve beyond point A represents the ballooning mode stability criterion.

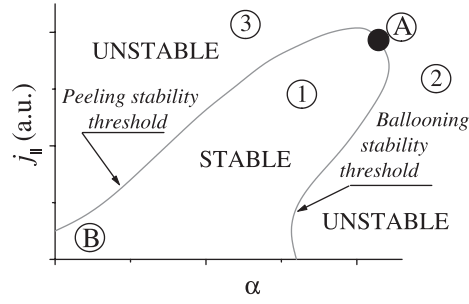


Figure 1. Schematic diagram of an ELM crash. The stable region ① separates two unstable regions ② and ③. In the region ②, the ELM crashes are caused by the ballooning instability; in the region ③, the ELM crashes are caused by the peeling instability. The ballooning–peeling threshold is shown as a function of the parallel component of current density, $j_{||}$ and the normalized pressure gradient, α . In general, the parallel component of plasma density destabilizes both the ballooning and peeling modes, and the pressure gradient stabilizes the peeling mode and destabilizes the ballooning mode.

In the current model, it is assumed that as soon as either the ballooning or the peeling mode criterion is satisfied at any point within the pedestal, an ELM crash occurs. Compared with the characteristic transport times, an ELM crash is an almost instantaneous event. During an ELM crash, plasma is removed from the edge region, which is typically several times wider than the width of the H-mode pedestal. In order to model the effect of an ELM crash, the plasma pressure is reduced by 70% in the ELM region. The changes in the plasma profiles caused by an ELM crash are computed in between the transport time steps. The transport model is not changed by the ELM crashes and the transport coefficients and fluxes are computed self-consistently from the transport model during the transport time steps. An alternative approach is used by Lönnroth *et al* [20–22, 42] and by Onjun *et al* [23, 24], in which the edge transport is transiently increased by a large amount in order to produce the rapid changes in the edge plasma profiles produced by each ELM crash. In this paper, each ELM crash is an instantaneous event on the transport time scale.

The width of the ELM region, Δ_{ELM} , is computed using an empirical scaling for the plasma energy removed by an ELM crash [38, 39]

$$\Delta_{\text{ELM}} \propto C_{\Delta} \left(\frac{\Delta W}{\nabla p_{\text{crit}}} \right)^{0.5}, \quad (16)$$

where ΔW is the energy loss during an ELM crash and C_{Δ} is a fitting coefficient. Since C_{Δ} depends on the minor and major radii, it can be considered to be a constant for any specific device. For the ASTRA simulations of the DIII-D tokamak, C_{Δ} is set to 0.1. The energy loss during an ELM crash is calculated using an empirical expression that has been obtained from analysis of the DIII-D data [43]:

$$\Delta W \propto W \left(\frac{S}{P_{\text{heat}}} \right)^{0.38} B_T^{-0.31}. \quad (17)$$

where S is the plasma area, P_{heat} is the auxiliary heating power and W is the plasma energy.

The model used by Lönnroth, Onjun and others in the JETTO code is different, and in some ways similar, when compared with the model used in the ASTRA code in this paper. The same peeling mode stability criterion is used both in the ASTRA and JETTO codes. The width of the pedestal is computed self-consistently using flow shear stabilization of the anomalous transport in the ASTRA code while the width of the pedestal is prescribed in the JETTO code

in [20–24]. In the ASTRA model, electron thermal transport is computed from the anomalous transport that remains (mostly from the ETG mode) after flow shear stabilization of the longer wavelength modes of turbulence, while in the JETTO model, electron thermal transport in the pedestal has been assumed to be equal to the neoclassical ion thermal transport computed at the top of the pedestal. Finally, the changes to the profiles caused by each ELM crash are implemented in different ways in the ASTRA and JETTO codes.

3. Testing the model with the ASTRA code

The models described above, for the reduction of anomalous transport in the pedestal and for the triggering of ELM crashes, are implemented in the ASTRA v. 5.2 (Automated System for Transport Analysis in a tokamak) transport code [29]. The four $\alpha_l^{(j)}$ coefficients in equation (8) can be used to calibrate the model.

During the initial step of the calibration, the objective is to reproduce major phenomena, such as the formation of H-mode pedestal, L–H transition and pedestal reconstruction after an ELM crash. The $\alpha_l^{(j)}$ coefficients should be large enough to suppress the transport at the plasma edge region to a level that is sufficient for the L–H transition to occur. The pedestal starts to form prior to the L–H transition. The values of the $\alpha_l^{(j)}$ coefficients that are necessary for the transition are higher than the values that are required for the pedestal formation. In addition, the ELM frequency is controlled through the calibration of the $\alpha_l^{(j)}$ coefficients. If the coefficients $\alpha_l^{(j)}$ are small, the normalized pressure gradient, α , does not exceed the critical value α_{cr} (see equation (14)), and the ballooning criterion for an ELM crash is not violated. With larger values of the $\alpha_l^{(j)}$ coefficients, the ELMs can be triggered more readily by the ballooning instability. Consequently, the ELM frequency is increased as the $\alpha_l^{(j)}$ coefficients are increased. (Of course, this logic does not necessarily apply to the ELMs that are triggered by the current driven peeling instability.) At the same time, the coefficients should not be so large that the anomalous transport is completely suppressed everywhere in the plasma. These limitations provide upper and lower bounds for the $\alpha_l^{(j)}$ coefficients.

The second step of the model calibration consists of the adjustment of the coefficients $\alpha_l^{(j)}$ in accordance with observed experimental dependencies and trends. For example, the ion temperature, in most cases, is observed to be higher than the electron temperature. This provides an additional constraint on the $\alpha_l^{(j)}$ coefficients. The model developed in this paper results from applying the first two steps of the calibration process. Some preliminary results of the model calibration that are associated with matching experimental dependencies and trends are discussed in section 4.

During the third step of model calibration, fine tuning of the $\alpha_l^{(j)}$ coefficients can be carried out. At this stage, the calibrated model is expected to reproduce the experimental plasma profiles in the plasma core and edge for different types of discharges and for different tokamak devices. This third step in the calibration of the model is beyond the scope of this paper.

A reference scenario for ASTRA simulations is based on the parameters of a DIII-D discharge [30]. Profiles from an analysis simulation of experimental data that are given in figure 2 are used. In particular, data are used for electron, ion and impurity density profiles (see figure 2(a)), toroidal rotational velocity, Z_{eff} (see figure 2(b)), the current density driven by the neutral beam injection (NBI) heating (see figure 2(c)), and the auxiliary heating power deposited to electrons and ions (see figure 2(d)). These profiles are prescribed and fixed in form. The experimental radial profile of total current density is used as an initial condition for the magnetic diffusion equation, which is solved in the ASTRA code. Other input parameters

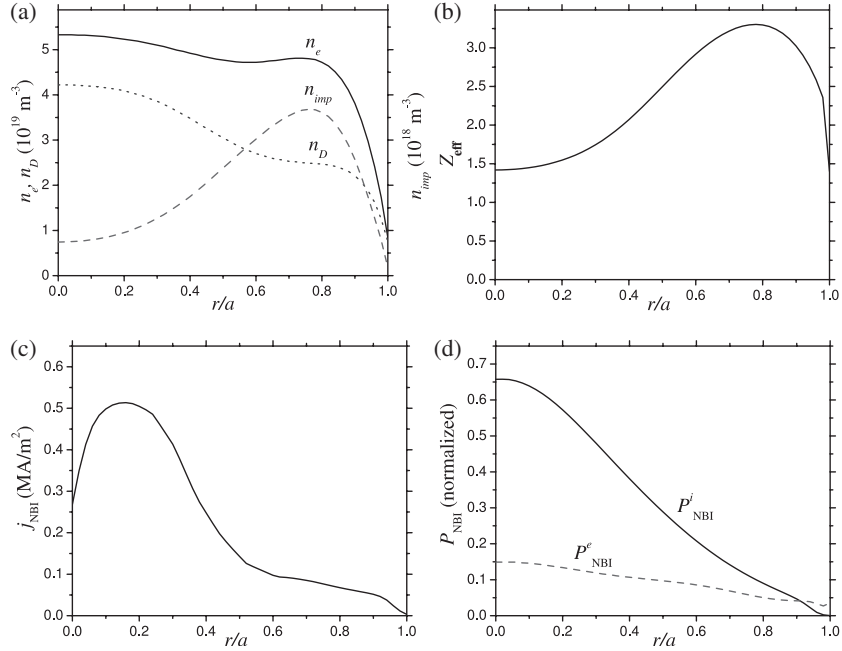


Figure 2. Profiles from an analysis simulation of experimental data, which are used in the simulations with the ASTRA code: (a) electron, ion and impurity densities, (b) Z_{eff} , (c) the current density driven by the NBI heating and (d) auxiliary heating power deposited to electrons and ions.

are the following: minor radius $a = 0.61$ m; major radius $R = 1.68$ m; toroidal magnetic field $B_T = 2.10$ T; plasma current $I = 1.54$ MA; line average density $\langle n_e \rangle = 4.84 \times 10^{19} \text{ m}^{-3}$; elongation $\kappa = 1.82$ and triangularity $\delta = 0.6$. The NBI auxiliary heating power deposited to electrons and ions in the simulation is increased from 1 MW to approximately 6 MW at 0.06 s, as shown in figure 3.

In the ASTRA simulation, the electron and ion temperatures are observed to increase after the heating power increases and the transition from L- to H-mode is observed at about 0.07 s. Also, the H-mode pedestal is formed at this time in both the electron and ion temperature profiles.

The radial electric field in the ASTRA simulation increases towards the edge of the plasma, reaching a maximum within the pedestal region and decreasing at the plasma edge. This sharp maximum has also been observed in experiments [44] and in numerical simulations [45–47]. The sharp peak in the radial electric field produces sufficiently high values of $\omega_{E \times B}$ flow shear rates to provide the necessary condition for the transition from the L- to the H-mode. Figure 4 shows the profile of the radial electric field and the $\vec{E}_r \times \vec{B}$ flow shear during the L-mode and the H-mode stages in the simulation. No bifurcation of the radial electric field in time during the discharge of the L–H transition is observed, which is consistent with the results of the numerical simulation [45, 46].

The L-mode is characterized by a large fluctuation level at the plasma edge. Large transient coherent structures are observed in the experiments [48]. The L–H transition occurs when the velocity shear becomes strong enough and the condition $\omega_{E \times B} > \gamma_{\text{max}}$ is satisfied. While this condition agrees with the $\vec{E}_r \times \vec{B}$ flow shear suppression function that is used in this study, a strong velocity shear can develop as a result of fast MHD activity, which is not always captured by transport codes. Moreover, transport codes usually do not handle coherent

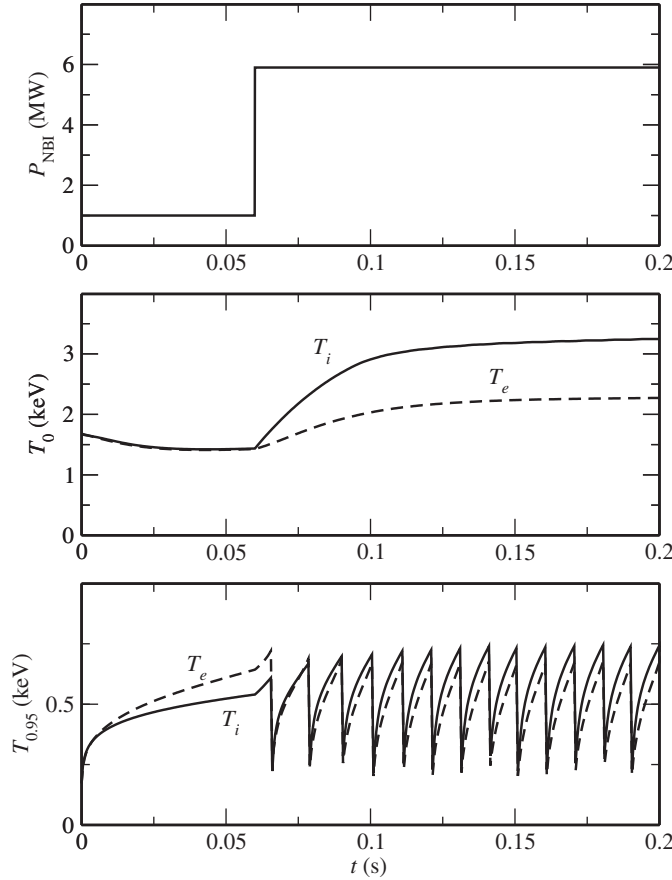


Figure 3. The NBI heating power absorbed by the ions and electrons as a function of time is shown in the top panel. The electron and ion temperatures from the ASTRA simulation are plotted as a function of time at the plasma centre and at $r/a = 0.95$ in the centre and bottom panels, respectively.

structures observed in experiments during L-mode. These structures are beyond the spatial and temporal scales that transport codes can resolve. Transport simulation can follow the L–H transition, but can not reproduce the sharp L–H transition in detail.

The total radial electric field (solid curve in the top panel) in figure 4 is used in the computation of the $\vec{E}_r \times \vec{B}$ flow shear rate (shown in the bottom panel), which, in turn, is used for the computation of the flow shear suppression functions for the ITG/TEM and resistive ballooning modes. (Note the difference in coordinate scale between the L-mode and the H-mode E_r plot.) In figure 4, the magnitudes of the diamagnetic (dashed curve) and poloidal (dotted curve) contributions to the total radial electric field are also shown. These contributions to the total electric field correspond to the first and second terms in equation (10). The sharp increase in the total radial electric field at the plasma edge is mainly the result of the diamagnetic contribution. At $t = 0.155$ s, the maximum radial electric field near the plasma edge during the H-mode stage is about three times the value of the radial electric field at $t = 0.001$ s, during the L-mode stage. As a result, the gradient dE_r/dr , which is involved in the calculation of the $\omega_{E \times B}$ flow shear rate (see equation (1)), is approximately two times larger during the H-mode than during the L-mode.

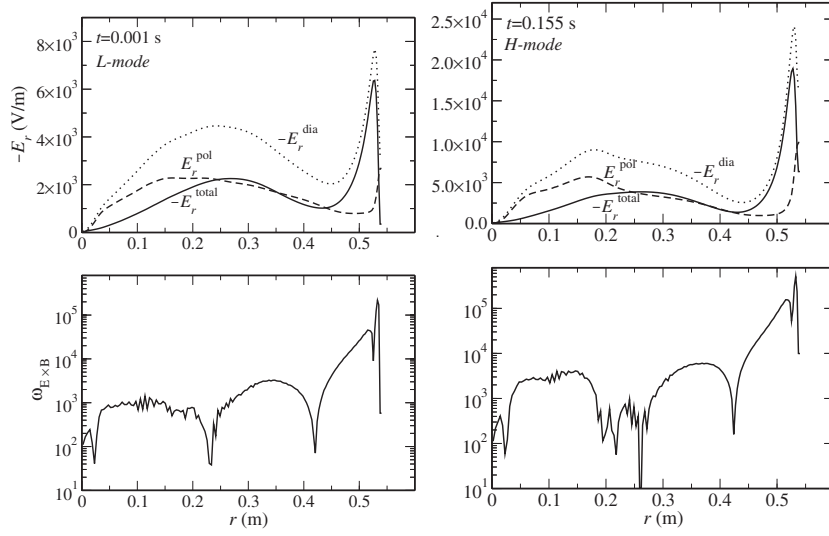


Figure 4. The radial electric fields and the $\omega_{E \times B}$ flow shear rate during the L-mode and the H-mode. The magnitudes of the diamagnetic (---) and poloidal (·····) components of the total radial electric field (—) are shown. These components correspond to the first and third terms in equation (10). Note that signs of these two terms in equation (10) are not included in this figure.

The resulting flow shear suppression functions, and their effect on the ion thermal diffusivities, are shown in figure 5. It is seen that without flow shear suppression (top panels), the resistive ballooning and the ITG contributions to the total ion thermal diffusivity do not change significantly from L- to H-mode. However, when flow shear suppression is taken into account (bottom panels), the resistive ballooning mode is suppressed more strongly in the H-mode than in the L-mode stage of the discharge. As a result, the resistive ballooning mode contributes less to the transport near the edge of the plasma in the H-mode than in the L-mode. Since the resistive ballooning mode usually contributes most at the plasma edge, the total thermal diffusivity is strongly reduced at the plasma edge in the H-mode and, consequently, temperature gradients become steeper and form a pedestal.

Each ELM crash in the model is considered as an instantaneous event, while recovery from each crash is an extended phenomena. Figure 6 shows the recovery from an ELM crash that occurs at 0.2005 s in the simulation. The profile is completely recovered and exhibits the H-mode pedestal at 0.2083 s. Note that the width of the region affected by ELMs is computed from the empirical relation given by equation (16) and, for the case shown in figure 6, the ELM width is about eight times wider than the H-mode pedestal width. The temperature profile in the plasma core is reduced somewhat while the pedestal rebuilds between ELM crashes.

Figure 7 shows the evolution of the bootstrap current as a function of normalized pressure gradient between two ELM crashes. The points represented by squares indicate the bootstrap current density and the circles represent the critical pressure gradient. Each pair of points represents a different time in the ELM cycle: points A and A' represent the first time step in an ELM cycle; points D and D', the time just prior to the next ELM crash and points E and E', the time just after the next ELM crash. The unprimed points represent the bootstrap current density and the primed points represent the value of the critical normalized pressure gradient, α_{cr} , associated with each time point during an ELM cycle. As the normalized pressure gradient increases from 3 to 11 along the horizontal axis and the bootstrap current density increases from 0.05 to 0.37 MA m⁻² along the vertical axis, the critical pressure gradient varies slightly, in

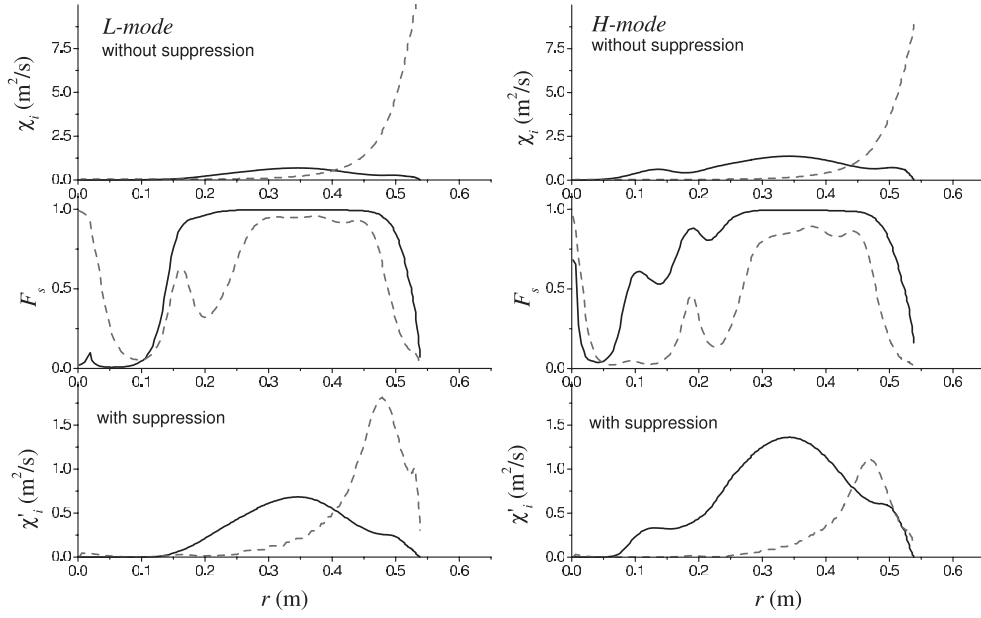


Figure 5. Radial profiles of ITG (—) and resistive ballooning (- - -) ion thermal diffusivities without flow shear suppression in L-mode and H-mode (top panel); shear suppression functions for ITG (—) and resistive ballooning (- - -) thermal transport (middle panel) and the resulting thermal diffusivities after including the $E_r \times B$ flow shear suppression (bottom panel).

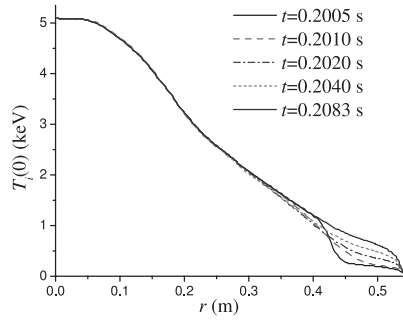


Figure 6. Ion temperature radial profile recovery after an ELM crash. Lower solid curve shows the temperature profile at the next time step after an ELM crash. Dashed and dotted curves show different stages of profile recovery after the crash. The upper solid curve shows the ion temperature profile completely recovered after an ELM crash.

the range from 11 to 11.7. At a time just beyond the time associated with point D, the pressure gradient in the edge region exceeds α_{cr} and an ELM crash occurs, resulting in the values of j_{bs} and α rapidly changing from those at point D to those at point E. The critical value of the normalized pressure gradient depends on the value of the magnetic shear in accordance with equation (14), which indirectly depends on the bootstrap current.

4. Initial comparison of simulations with experimental scalings

In this section, the results of the simulations are compared with observed experimental dependencies and trends. Agreement with experimental trends can provide some of the

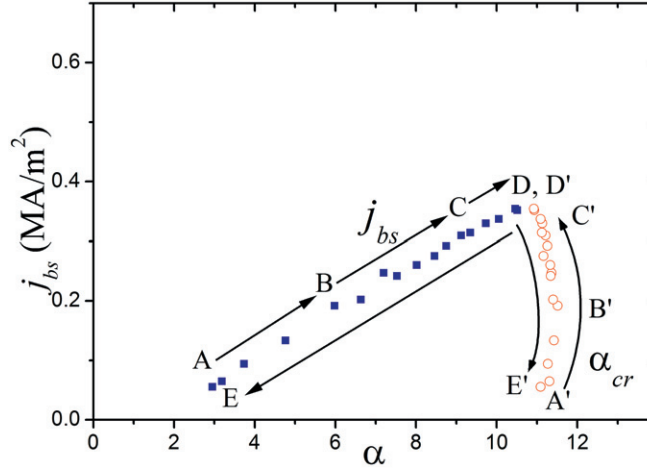


Figure 7. Illustration of the variation of bootstrap current (■) and critical plasma pressure gradient (○) between two consecutive ELM crashes. Each pair of points represents different time during an ELM cycle: points A and A' represent the first time step during an ELM cycle; points D and D', the time prior to the next ELM crash; points E and E', the time just after the next ELM crash. The primed points represent the value of the critical pressure gradient for a specific time, and the unprimed points represent the bootstrap current density.

(This figure is in colour only in the electronic version)

AQ2

necessary justification for the assumptions used in the model. In this paper, scans with heating power, magnetic field and plasma density are considered. In the reference scenario, all ELM crashes are caused only by the ballooning instability, even though both ballooning and peeling criteria are implemented in the ASTRA code. The simulations with both criteria implemented are rather slow, because a detailed equilibrium computation with small time steps is required for the peeling condition given in equation (15). Consequently, in the scans that are considered in this section, only the ballooning condition is used to trigger ELM crashes. An example of a simulation with both the peeling and the ballooning conditions included is presented in section 5. Another possible model is one in which the equilibrium evolves along the α_{cr} boundary until $j > j_{cr}$ and the peeling mode is triggered.

4.1. Scan with heating power

In the scan over auxiliary heating power, the auxiliary heating power is varied from 3.5 to 7.0 MW in a series of simulations. In figure 8, the electron, ion and average electron-ion, $(T_e + T_i)/2$, temperatures at the top of the pedestal just before an ELM crash and the ELM frequency are shown as a function of the auxiliary heating power. The ELM frequency is observed to increase with the heating power in the simulations, which is consistent with experimental observations in H-mode plasmas with type I ELMs. The temperatures at the top of the pedestal have a weak dependence on the heating power in the simulations. For example, as shown in figure 8, the simulation result scaling, that describes the dependence of the average pedestal temperature on heating power, is given by

$$\frac{T_e + T_i}{2} \propto P_{\text{heat}}^{0.18}. \quad (18)$$

This result is consistent with experimental observations, where it is found that

$$T_{\text{ped}} \propto P_{\text{heat}}^\alpha, \quad (19)$$

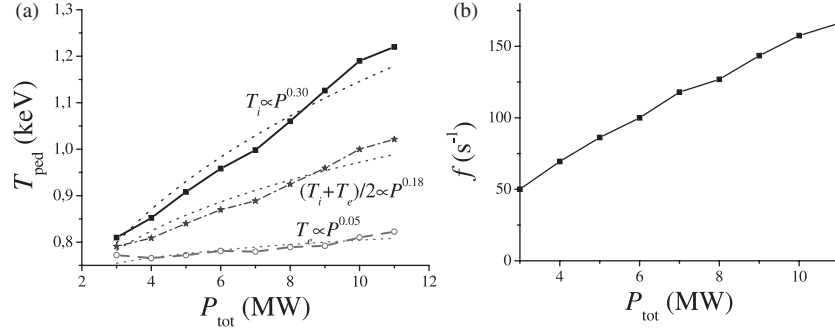


Figure 8. Pedestal temperatures and ELM frequency in the heating power scan. The dotted lines in panel (a) show the power dependence scaling curves that provide the best fit to the simulation results.

with α in the range $0.0 \leq \alpha \leq 0.5$. The ELM crash frequency is observed to increase with increasing auxiliary heating power (see figure 8(b)). If the ELM crashes are triggered by a critical pressure gradient that is proportional to the magnetic shear in the pedestal, then the temperature at the top of the pedestal slowly increases with increasing heating power. The reason for this effect is that the current density in the pedestal has less time to rebuild between ELM crashes as the ELM crashes become more frequent, and, consequently, the magnetic shear, s , and the critical pressure gradient, α_{cr} , remain at high levels in the pedestal between ELM crashes. The critical pressure gradient, α_{cr} , increases during each ELM crash because of its dependence on the magnetic shear, s . Each ELM crash removes most of the bootstrap current density from the pedestal. As a result, the current density in the pedestal decreases after each ELM crash and then increases as the bootstrap current rebuilds before the next ELM crash. The magnetic shear in the pedestal, which is inversely related to the current density, increases after each ELM crash and then decreases before the next ELM crash. Consequently, α_{cr} increases slightly and then decreases slightly during each ELM cycle. Since inductive effects impede the rebuilding of the pedestal current density, the normalized pressure gradient, α , can rebuild much faster than the increase in the pedestal current density and the resulting decrease in α_{cr} . That is why the critical pressure gradient, α_{cr} , remains at a higher level when ELMs are more frequent.

As the heating power is increased, the heat flux through the pedestal increases and the pressure gradient in the pedestal rebuilds more rapidly between ELM crashes. Consequently, there are more frequent ELM crashes at higher heating power, and, for the reasons described earlier, the critical pressure gradient, α_{cr} , increases moderately. The higher value of the critical pressure gradient implies that the plasma pressure and temperature can reach higher values before an ELM crash occurs. This effect is demonstrated in figure 9, which shows the evolution of the ion temperature and bootstrap current density at 0.95 of the minor radius. Figures 9(a) and (c) correspond to the case of the lower heating power (3 MW) and lower ELM frequency and figures 9(b) and (d) correspond to the case of the higher heating power (11 MW) and higher ELM frequency, where the current density in the pedestal region does not rebuild completely between successive ELM crashes.

4.2. Scan with magnetic field

In the magnetic field scan, the magnetic field is varied from 2.1 to 4.6 T. Since the safety factor is fixed in this scan, the poloidal and toroidal components of the magnetic field are varied in the

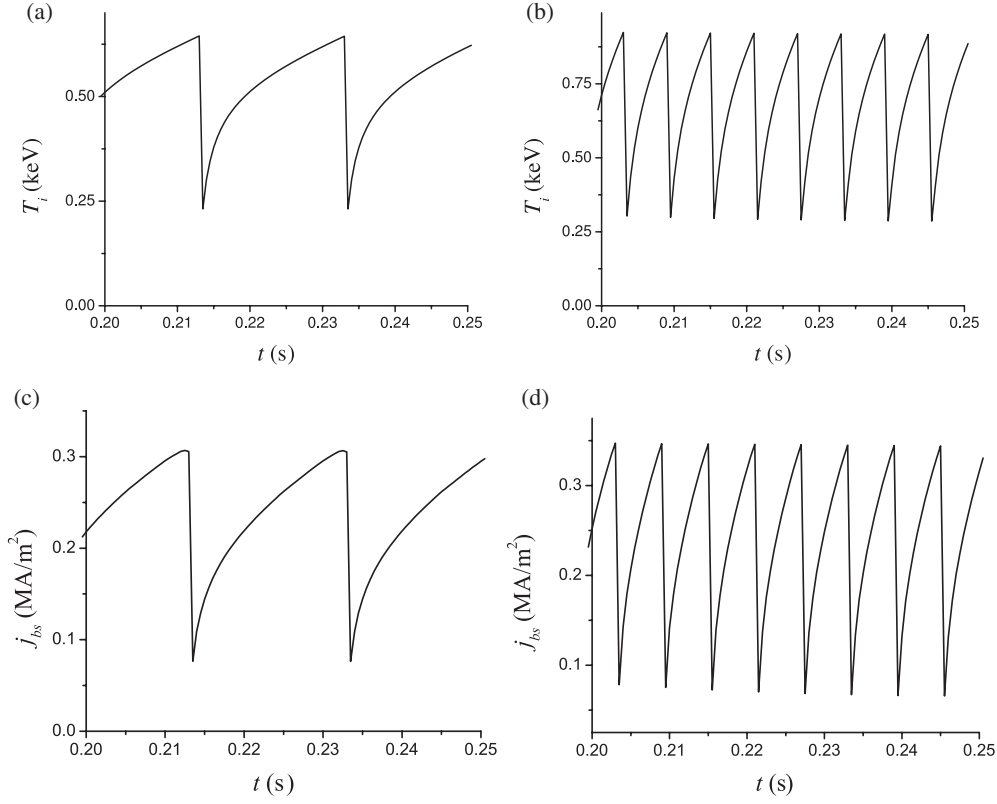


Figure 9. Evolution of the ion temperature and bootstrap current density at 0.95 of the minor radius for lower (a) and (c) and higher (b) and (d) total heating powers.

same way. The pressure gradient would remain fixed if the normalized pressure gradient, α , were fixed in this scan. The dependencies of the electron and ion pedestal temperatures, and the ELM frequency on the magnetic field are shown in figure 10. It can be seen in figure 10(a) that the pedestal temperature slowly increases as the magnetic field increases. This result is consistent with the weak $B_T^{0.32}$ scaling found in the empirical fit to experimental data in [49] for type-1 ELMy H-mode discharges when the plasma current is held fixed (as is the case in this simulation scan). The dependence of the pedestal temperature on the magnetic field in the simulations results from the pedestal width dependence on the magnetic field, which is observed in this scan. The pedestal width decreases with the magnetic field. This leads to higher values of magnetic shear at the top of the pedestal, and consequently to higher values of critical pressure gradient, α_{cr} . This explanation is valid as long as the plasma is in the first ballooning stability limit. In the second ballooning stability limit, the dependence of the ballooning instability threshold, α_{cr} , on the magnetic shear is reversed and the pedestal temperature will decrease with the magnetic field.

Figure 10(b) shows the dependence of the ELM frequency on the magnetic field. The ELM frequency decreases with increasing magnetic field, a trend similar to the one observed in experimental data. This observation has a simple explanation. Since the neoclassical transport, which is inversely proportional to the square of the poloidal magnetic field, is a main transport mechanism within the pedestal, the pedestal can recover faster after each ELM crash in plasmas with stronger poloidal magnetic field compared to the recovery in plasmas with

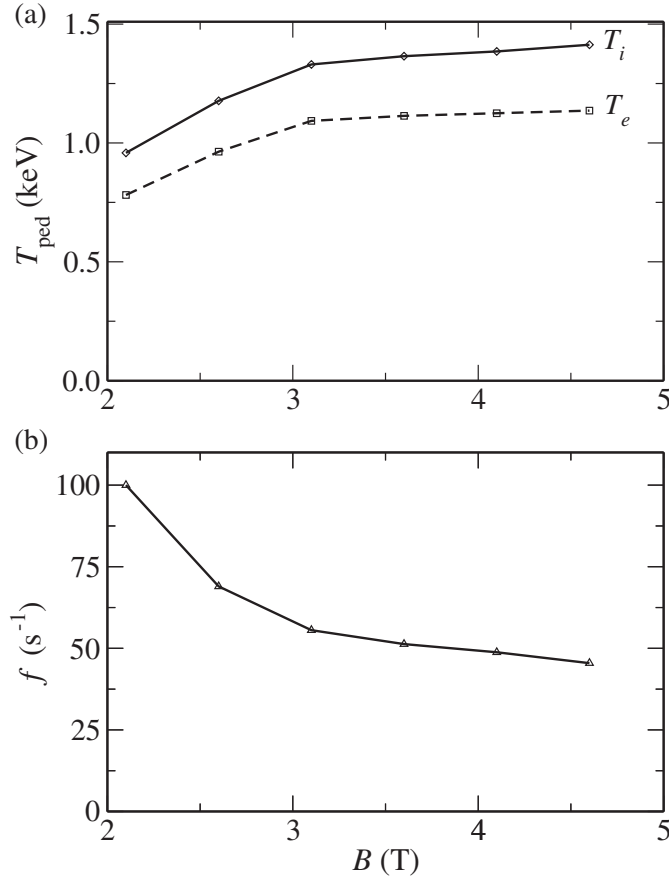


Figure 10. Simulation results showing the dependence of pedestal temperatures and frequency of ELM crashes on the magnetic field.

weaker magnetic field. Also, the anomalous transport will be weaker when the magnetic field is stronger. In particular, the resistive ballooning thermal diffusivities are inversely proportional to the square of the toroidal magnetic field:

$$\chi_{\text{RB}}^{\text{i,e}} \propto \frac{q^2}{B_\phi^2}.$$

As a result, the ELM frequency is higher in a stronger magnetic field plasma.

4.3. Scan with plasma density

Experimental observations indicate that pedestal characteristics are strongly dependent on the plasma density. It is observed that the electron and ion temperatures at the top of the pedestal decrease with increasing plasma density. Different experiments suggest different plasma density scalings, but all the scalings are in the range

$$T_{\text{i,e}} \propto \frac{1}{n_e^\alpha}, \quad (20)$$

where $\alpha \approx 1$ [25]. Also, the frequency of ELMs is observed to increase with the plasma density [50]. In a series of ASTRA simulations, the plasma density is changed from

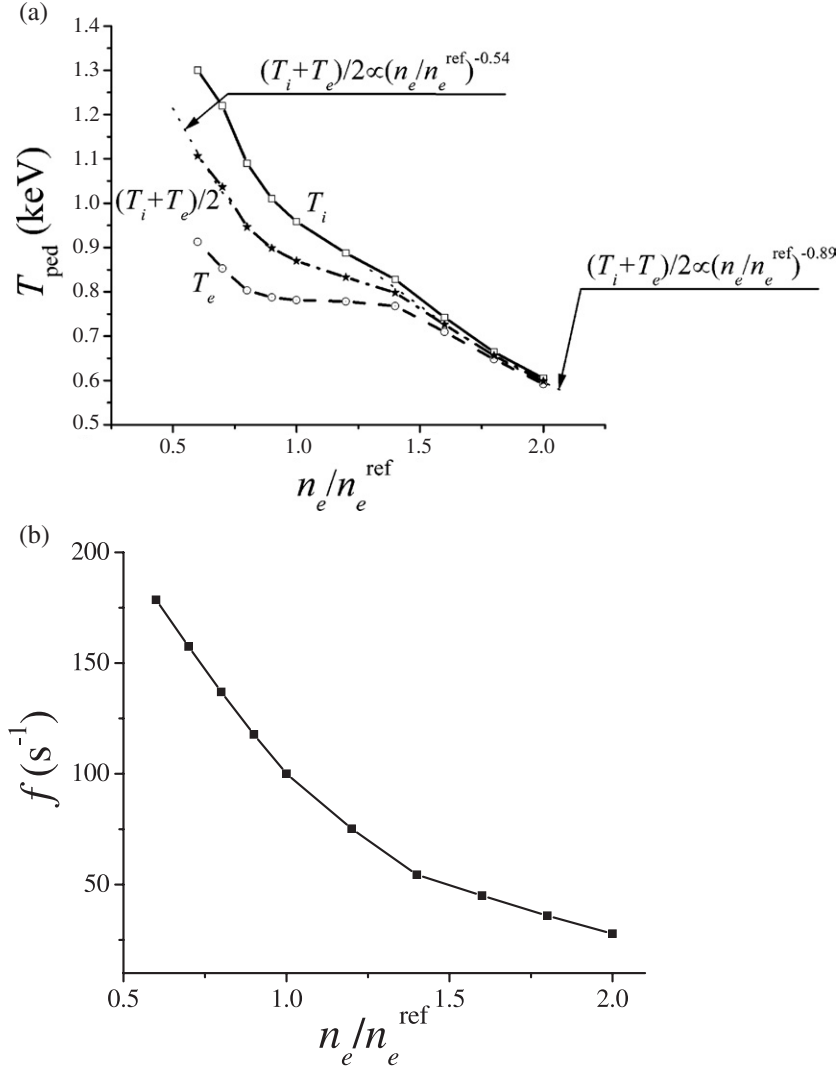


Figure 11. Pedestal temperatures and frequency of ELM crashes in the density scan. Dotted lines in panel (a) show two curves that fit the average temperature at the top of the pedestal in the limits of low and high densities.

0.6 to 2.0 times the reference density used in the simulations described earlier, $n_e^{\text{ref}} \equiv \langle n_e \rangle = 4.84 \times 10^{19} \text{ m}^{-3}$. The simulation results shown in figure 11 indicate how the electron, ion and average temperatures, $(T_e + T_i)/2$, at the top of the pedestal vary with plasma density (in panel (a)), and how the ELM frequency varies with the plasma density (in panel (b)). The electron and ion temperatures have different scalings at low and high densities. The average temperature at the top of the H-mode pedestal is found to vary with plasma density as

$$\frac{T_e + T_i}{2} \propto \frac{1}{n_e^{0.54}} \quad \text{at lower densities: in the range from 0.6 to 0.8 of } n_e^{\text{ref}}$$

and

$$\frac{T_e + T_i}{2} \propto \frac{1}{n_e^{0.89}} \quad \text{at higher densities: in the range from 1.4 to 2.0 of } n_e^{\text{ref}}.$$

The values of the electron and ion temperatures at the top of the pedestal tend to become nearly equal as the plasma density increases, as might be expected as a consequence of increased collisionality. The scaling of the electron temperature changes more strongly than the scaling of the ion temperature as the plasma density is increased. This might be caused by the effect of ETG modes, which are not suppressed by the $\vec{E}_r \times \vec{B}$ flow shear. It should be noted, however, that the observed temperature scalings with the plasma density are likely to change somewhat when particle transport is implemented.

The results of the simulations show that the ELM frequency decreases with increasing plasma density, which is not consistent with experimental observations. This inconsistency reveals two important limitations of the model in its present form. The first limitation is related to the influence of the density profiles on the results. It is found that the simulations show a strong dependence of the ELM amplitude and ELM frequency on the width of the density pedestal and on the density gradients in the pedestal region. By doubling the width of the density pedestal, the ELM frequency is reduced by a factor of two and the ELM amplitude is increased by more than a factor of three. In this paper, the density profile is unchanged during all the simulations; whereas, in some experiments, the density profiles are observed to change more rapidly and more completely than the temperature profiles during each ELM crash. In order to use the combined model for pedestal and ELMs in a more complete predictive transport simulation, it is required that particle transport and the effect of ELM crashes on the density profiles be implemented. A second limitation of the model, used to present the results in this paper, is related to the expression for the critical value of the normalized pressure gradient given by equation (14). This expression is valid in the first ballooning stability limit. It is likely, however, that the plasma will move to the second stability region if the plasma density is reduced, since that decreases the collisionality, which increases the bootstrap current and decreases the magnetic shear in the pedestal [42]. This limits the applicability of this model to the cases in which the parametrized dependence for α_{cr} remains in the first ballooning stability limit.

5. Discussions and conclusions

A new combined model for the pedestal and ELMs is presented. The model is used to self-consistently compute the L–H transition, the pedestal width, height, shape, the frequency of ELMs and the ELM amplitude. The width of the ELM crashes is taken from the empirical scalings, and the conditions for ELM triggering are based on MHD stability analysis. The model is tested using the ASTRA transport code. The formation of the H-mode pedestal and the L–H transition is predicted as a consequence of the $\vec{E}_r \times \vec{B}$ flow shear suppression alone. No additional contribution due to the magnetic shear is used here; future comparison calculations with differing magnetic configurations will show whether additional contributions are required. A DIII-D discharge [30] is employed as a reference case and a pedestal model is used to examine the dependence of the model results on plasma heating power, magnetic field and density using simulations in which plasma parameters are systematically varied from the reference case. The scalings obtained from the three scans are compared with the experimental observations.

Both the peeling and ballooning criteria for ELM crashes are implemented in the ASTRA code. However, a detailed equilibrium computation with small time steps and a reliable equilibrium package are required for the peeling condition given in equation (15). As result, simulations with both criteria for ELM crashes are rather slow. It has been verified using a stability code that all ELM crashes are caused by the ballooning instability in the reference scenario. Consequently, only the ballooning criterion is used in the plasma heating power,

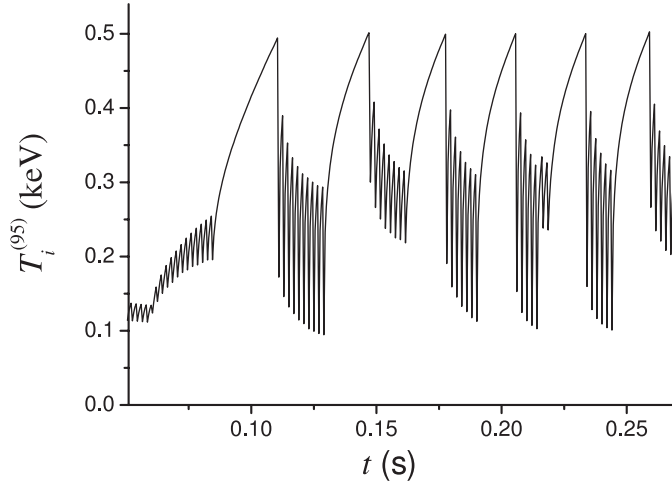


Figure 12. Evolution of the ion temperature at 0.95 of the minor radius in the ASTRA simulation where ELMs are triggered by both the peeling and ballooning modes (minor radius $a = 0.56$ m, major radius $R = 0.77$ m, toroidal magnetic field $B_T = 1.1$ T and plasma current $I = 1.538$ MA).

magnetic field and density scans that are presented in this paper. However, the inclusion of peeling trigger for ELM crashes can introduce new effects. An example of a scenario that is observed in the ASTRA simulations, with both peeling and ballooning conditions included for a low aspect ratio geometry and plasma parameters that differ from the geometry and plasma parameters of the reference case, is shown in figures 12 and 13. In this example, an initial ELM crash, caused by the ballooning mode instability, is followed by a series of frequent ELM crashes, shown in figure 12, caused by the peeling mode instability. This is in contrast to the sequence of ELM crashes described in figure 7 where the initial ELM crash resulting from a ballooning instability is followed by a subsequent ELM crash resulting from the same instability. Possible differences in sequences of ELM crashes are discussed below.

The pressure gradient decreases after an ELM crash caused by a ballooning mode instability. If the decrease is such that the plasma returns to the stable region 1 shown in figure 1, the pressure gradient rebuilds, and a subsequent ballooning mode ELM crash results, as illustrated in figure 7. However, if the decrease in pressure gradient is sufficient, the plasma can fall into the unstable region 3 in figure 1 where the condition for peeling instability given by equation (15) is satisfied. As a consequence, an ELM crash caused by the peeling instability follows immediately after the ELM crash caused by the ballooning instability. A series of frequent peeling ELM crashes can be observed in the simulations. These crashes depend on the evolution of the current density during the ELM crashes. When the edge current density is reduced to a sufficiently low value so that the criterion for the peeling mode instability is no longer satisfied, the pedestal pressure gradient rebuilds until an ELM crash results from the ballooning mode instability.

Figure 13 illustrates a scenario involving multiple peeling crashes between two ballooning crashes. The initial large ELM crash caused by the ballooning instability is followed by a series of small and frequent ELM crashes caused by the peeling instability. There is a lower stability limit value in the parallel component of the edge plasma current (about 0.2 MA m^{-2} for the case shown in figure 13), which corresponds to the point B on the diagram shown in figure 1. As soon as the edge plasma current density decreases below this value, there are no further ELM crashes resulting from the peeling mode. Then the edge plasma pressure gradient

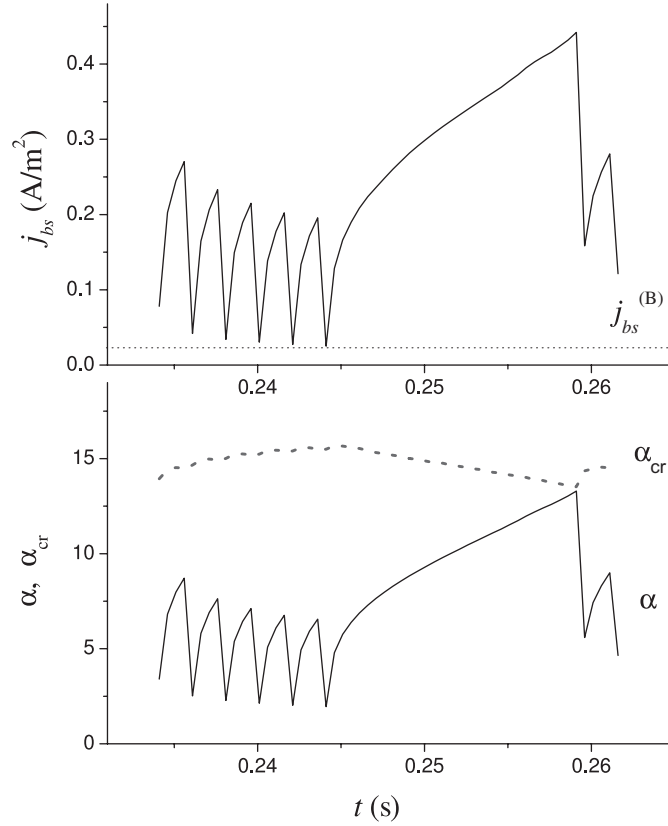


Figure 13. Evolution of the bootstrap current and plasma pressure gradient at the top of the pedestal between two consequent ELM crashes caused by the ballooning instability.

and the edge current density increases until the ballooning condition for an ELM crash is attained. In this scenario, the period between two consequent ELM crashes that are caused by the ballooning instability is much longer than if there were no peeling mode instabilities.

There are some natural limitations in transport codes. Transport models are extremely fast and provide an excellent tool for predictive studies of tokamak plasmas. However, transport codes deal with specific time and length scales and cannot completely describe very fast- or very short-scale effects. While the ASTRA code is successfully used in this paper to model the H-mode pedestal build up and to recover the plasma profiles after ELM crashes, it is difficult to expect to be able to reproduce the details of the very fast ELM crashes. Also, transport codes usually do not follow MHD modes and coherent structures that are observed in L-mode experiments, which might be important for the L–H transition. Consequently, it is difficult to reproduce the very sharp and fast L–H transition observed in experiments. However, the bifurcational nature of L–H transition can be mimicked by introducing a threshold in the flow shear suppression function given in equation (8):

$$F_l^{(j)} = \frac{1}{1 + \alpha_l^{(j)} (\omega_{E \times B} \tau_{lj})^2 H(\omega_{E \times B} - \gamma_{\max}^{lj})}, \quad (21)$$

where H is the step function. This idea will be tested in future studies.

This study is a step in the development of a new refined model for the pedestal and ELMs. In order to use the model within integrated predictive simulations, particle transport

should be implemented in addition to the thermal transport. Of the scans considered in this paper, the plasma density scan is expected to be affected the most from the inclusion of the particle transport. This might resolve the observed discrepancies between the experimental and simulated scalings of ELM frequency and electron and ion temperatures at the top of the H-mode pedestal as a function of the plasma density. A more general stability criterion that includes the first and second stability limits should be derived and used in the model for the ELM trigger. Such a parametrization requires a detailed stability analysis. Finally, a calibration of the model against experimental data will be the subject of future studies. However, at the present stage of development, simulation results agree qualitatively with some experimental dependencies. For example, by using the combined pedestal ELM model, it is found that the temperatures at the top of the pedestal decrease with increasing plasma density and decreasing heating power, and that the ELM frequency decreases with increasing magnetic field and decreasing heating power.

Acknowledgments

The authors thank Dr V Parail for useful discussions and his valuable support and Dr G Pereverzev for installation and support of the ASTRA code. This work is supported by US DOE contract DE-FG02-92ER-5414.

References

- [1] Connor J W and Wilson H R 1994 *Plasma Phys. Control. Fusion* **36** 719
- [2] Bécoulet M *et al* 2003 *Plasma Phys. Control. Fusion* **45** A93
- [3] Stacey W 2004 *Phys. Plasmas* **11** 1511
- [4] Lehnert B 1966 *Phys. Fluids* **9** 1367
- [5] Hamaguchi S and Horton W 1992 *Phys. Fluids B* **4** 319
- [6] Hahm T S and Burrell K H 1995 *Phys. Plasmas* **2** 1648
- [7] Burrell K H 1997 *Phys. Plasmas* **4** 1499
- [8] Staebler G M, Waltz R E and Wiley J C 1997 *Nucl. Fusion* **37** 287
- [9] Zhu P, Bateman G, Kritz A H and Horton W 2000 *Phys. Plasmas* **7** 2898
- [10] Shaing K C, Crume E C Jr and Houlberg W A 1990 *Phys. Fluids B* **2** 1492
- [11] Zhang Y Z and Mahajan S M 1992 *Phys. Fluids B* **4** 1385
- [12] Figarella C F, Benkadda S, Beyer P, Garbet X and Voitsekrovitch I 2003 *Phys. Rev. Lett.* **90** 015002
- [13] Zolotukhin O V, Igitkhanov Y, Janeschitz G, Pacher G W, Pacher H D, Pereverzev G V, Strohmayer G and Sugihara M 2001 *28th EPS Conf. on Controlled Fusion and Plasma Physics (Funchal, Portugal, June 2001)* pp 677–80
- [14] Janeschitz G *et al* 2002 *Plasma Phys. Control. Fusion* **44** A459
- [15] Pacher G *et al* 2004 Operating window of ITER from consistent core-pedestal-sol modelling with modified MMM transport and carbon *Plasma Phys. Control. Fusion* at press
- [16] Sugihara M, Igitkhanov Y, Janeschitz G, Hubbard A E, Kamada Y, Lingertat J, Osborne T H and Suttrop W 2000 *Nucl. Fusion* **40** 1743
- [17] Hahm T S and Diamond P H 1987 *Phys. Fluids* **30** 133
- [18] Bateman G, Kritz A H, Kinsey J E, Redd A J and Weiland J 1998 *Phys. Plasmas* **5** 1793
- [19] Voitsekrovitch I *et al* 1999 *Phys. Plasmas* **6** 4229
- [20] Lönnerth J-S *et al* 2004 *Plasma Phys. Control. Fusion* **46** A249
- [21] Lönnerth J-S *et al* 2004 *Plasma Phys. Control. Fusion* **46** 1197
- [22] Lönnerth J-S *et al* 2004 *Plasma Phys. Control. Fusion* **46** 767
- [23] Onjun T, Kritz A H, Bateman G, Parail V, Wilson H, Lönnerth J, Huysmans G and Dnestrovskij A 2004 *Phys. Plasmas* **11** 1469
- [24] Onjun T *et al* 2004 *Phys. Plasmas* **11** 3006
- [25] Onjun T, Bateman G, Kritz A H and Hammett G 2002 *Phys. Plasmas* **9** 5018
- [26] Kritz A H *et al* 2003 *Proc. 30th Eur. Conf. on Controlled Fusion and Plasma Physics (St Petersburg, 2003)* (Geneva: European Physical Society)

AQ3

-
- [27] Bateman G *et al* 2003 *Phys. Plasmas* **10** 4358
- [28] Schneider R *et al* 2004 Comprehensive suite of codes for plasma-edge modeling *Comput. Phys. Commun.* at press
- [29] Pereverzev G and Yushmanov P N 2002 ASTRA automated system for transport analysis in a tokamak *Technical Report IPP 5/98*, Max-Planck Institut für Plasmaphysik
- [30] Murakami M *et al* 2000 *Nucl. Fusion* **40** 1257
- [31] Nordman H, Weiland J and Jarmén A 1990 *Nucl. Fusion* **30** 983
- [32] Weiland J and Hirose A 1992 *Nucl. Fusion* **32** 151
- [33] Guzdar P N, Drake J F, McCarthy D and Hassam A B 1993 *Phys. Fluids B* **5** 3712
- [34] Horton W *et al* 2000 *Phys. Plasmas* **7** 1494
- [35] Houlberg W A, Shaing K C, Hirshman S P and Zarnstorff M C 1997 *Phys. Plasmas* **4** 3230
- [36] Guzdar P N, Kleva R G, Das A and Kaw P K 2001 *Phys. Rev. Lett.* **87** 015001
- [37] Kim Y B, Diamond P H and Groebner R J 1991 *Phys. Fluids B* **3** 2050
- [38] Zohm H 1996 *Plasma Phys. Control. Fusion* **38** 105
- [39] Connor J W 1998 *Plasma Phys. Control. Fusion* **40** 531
- [40] Lao L L 2000 *Plasma Phys. Control. Fusion* **42** A51
- [41] Wilson H *et al* 2000 *Nucl. Fusion* **40** 713
- [42] Lönnerth J-S *et al* 2003 *Plasma Phys. Control. Fusion* **45** 1689
- [43] Osborne T *et al* 1997 *Proc. 24th Eur. Conf. on Controlled Fusion and Plasma Physics (Berchtesgaden, 1997)* vol 21A (Geneva: European Physical Society) p 1701
- [44] Gohil P, Burrell K H and Carlstrom T N 1998 *Nucl. Fusion* **38** 93
- [45] Kiviniemi T P *et al* 2003 *Phys. Plasmas* **10** 2604
- [46] Heikkinen J A, Kiviniemi T P and Peeters A G 2000 *Phys. Rev. Lett.* **84** 487
- [47] Rozhansky V A, Voskoboynikov S P, Kaveeva E G, Coster D P and Schneider R 2001 *Nucl. Fusion* **41** 387
- [48] McKee G R *et al* 2003 *Phys. Plasmas* **10** 1712
- [49] Cordey J G for the ITPA H-mode Database Working Group and the ITPA Pedestal Database Working Group 2003 *Nucl. Fusion* **43** 670
- [50] Saibene G *et al* 1999 *Nucl. Fusion* **39** 1133

QUERIES

Page 1

AQ1

Please check if the affiliation and deletion of present address for 'Pankin' and 'Voitsekhovitch' is ok?

Page 13

AQ2

Please be aware that the colour figure 7 in this article will only appear in colour in the web version. If you require colour in the printed journal and have not previously arranged it, Please contact production editor now.

Page 21

AQ3

Please provide volume and page numbers for Refs. [15 and 28].